remote sensing

MDPI

Article

Feasibility of Ceilometers Data to Estimate Radiative Forcing Values: Application to Different Conditions around the COVID-19 Lockdown Period

Ruben Barragan [1,*], Francisco Molero [1], María José Granados-Muñoz [2,3], Pedro Salvador [1], Manuel Pujadas [1] and Begoña Artíñano [1]

[1] Department of Environment, Centro de Investigaciones Energéticas, Medioambientales y Tecnológicas (CIEMAT), Avda Complutense, 40, 28040 Madrid, Spain; f.molero@ciemat.es (F.M.); pedro.salvador@ciemat.es (P.S.); manuel.pujadas@ciemat.es (M.P.); b.artinano@ciemat.es (B.A.)

[2] Department of Applied Physics, Faculty of Sciences, University of Granada, Fuentenueva s/n, 18071 Granada, Spain; mjgranados@ugr.es

[3] Andalusian Institute for Earth System Research (IISTA-CEAMA), Avda. del Mediterráneo s/n, 18006 Granada, Spain

* Correspondence: ruben.barragan@ciemat.es; Tel.: +34-914962603

Received: 2 October 2020; Accepted: 9 November 2020; Published: 11 November 2020

Abstract: In this study, the feasibility of using ceilometer signals to retrieve radiative forcing values is evaluated. The Global Atmospheric Model (GAME) radiative transfer model is used to estimate the shortwave and longwave radiative forcing using an aerosol parameterization based on AERONET data and vertical profiles from a Lufft CHM-15k Nimbus ceilometer. First, eight cases confirmed as dusty days are analyzed to check the feasibility of using ceilometer profiles to feed GAME. The obtained radiative forcing estimates are in good agreement with the literature showing negative values in the short wave (SW) (cooling effect) and positive values in the long wave (LW) (heating effect), both at all levels. As in the literature, radiative forcing estimates show a strong dependence on variations in the aerosol optical depth (AOD), solar zenith angle (θ_z), surface temperature (ST), and single scattering albedo at 440 nm (SSA_{440}). Thus, GAME can be fed using ceilometer measurements obtaining reliable results. Then, as the temporal evolution of the AOD_{440} between 27 January and 15 June compared to the 6-year weekly AERONET AOD_{440} average (from 2014 to 2019) shows a decrease because of the lockdown imposed in Spain due to the COVID-19, a total of 37 radiative forcing calculations without African dust, divided into 8 scenarios, are performed in order to check the effect of the lockdown measures in the radiative forcing. It is shown that the decrease in the AOD, during the lockdown, caused a decrease in the cooling effect in the SW spectral range at all levels. Besides, the increase in the ST increased the heating effect of the aerosols in the LW at the top of the atmosphere and the presence of pollution and absorbing particles ($SSA_{440} < 0.90$) caused an increase of the heating effect in the LW at the surface. Therefore, the observed variations in the radiative forcing estimates before and during the lockdown are directly related with the decrease in emissions of aerosols related to human activities.

Keywords: radiative forcing estimates; aerosols; ceilometer signals; lockdown; COVID-19; sanitary crisis

1. Introduction

Natural and anthropogenic atmospheric aerosols cause great effects in many atmospheric processes, for instance, hydrological cycle, cloud cover, precipitations, and atmospheric radiative budget [1]. Therefore, anomalous atmospheric situations, in terms of air quality, might also have significant

consequences in terms of radiative forcing, which is directly related to aerosol optical and microphysical characteristics [2].

Local aerosol radiative forcing is estimated by means of radiative transfer models (RTM), such as SBDART [3], Streamer [4], MODTRAN [5], libRadtran [6], or the Global Atmospheric Model (GAME) [7,8]. The aerosol optical properties used as input in the RTMs can be retrieved from experimental measurements in the short wave (SW) spectral range. However, as the current remote sensing techniques do not allow direct retrieval of all the necessary data for the long wave (LW) spectral range, data should be retrieved from light scattering codes or consulted in tables [2]. In spite of this difficulty, radiative forcing in the LW cannot be neglected in radiative forcing calculations because it has been demonstrated that this component can reach between a fifth and a quarter of the SW radiative forcing at all levels [2,9,10]. Moreover, in both SW and LW spectral ranges, because of their significant influence, some specific atmospheric parameters not directly related to the aerosols such as relative humidity profile, surface albedo, or surface temperature that can be retrieved from satellite or radiosonde data, must also be taken into account.

There are many studies in the literature focused on the estimation of the aerosol radiative forcing during African dust outbreaks in several Mediterranean sites (see, e.g., in [1,2,10–16]). In general, data used in those studies come from intensive measurement campaigns; thus, they are generally valid only locally [9,17]. Therefore, observational networks acquire great importance for the spatial characterization of aerosol properties. As an example, the global Aerosol Robotic NETwork (AERONET; http://aeronet.gsfc.nasa.gov/) [18–20], which has robotic sun and sky photometers deployed worldwide, is one of the recognized instruments for the retrieval of column-integrated aerosol properties or the European Aerosol Research Lidar Network (EARLINET) [21], included in the European Research infrastructure for the observation of Aerosol, Clouds and Trace Gases (ACTRIS). Light detection and ranging (Lidar) systems are well-known active remote sensing instruments for the vertically resolved characterization of aerosol optical and microphysical properties [22], besides the ones belonging to EARLINET are advanced systems with elastic (355, 532, and 1064 nm) and Raman (387 and 607 nm) channels, the so-called 3 + 2 configuration; besides, some of them present depolarization capabilities and water vapor channels.

In addition, satellite measurements, such as those performed by CALIOP (Cloud-Aerosol Lidar with Orthogonal Polarization) [23] or MODIS (MODerate resolution Imaging Spectroradiometer) [24], can provide spatial coverage that may improve the determination of aerosol radiative effects at regional [12,25–27] or global scales [28,29]. However, the poorer temporal resolution of satellite measurements in comparison with ground-based instruments is not enough to study down to the last detail the temporal evolution of the atmosphere at local or regional scale, for instance, CALIPSO overpasses every AERONET or EARLINET site only two times each 16 days. This temporal gap can be covered by unmanned-unattended instruments that are not as advanced as the EARLINET Lidars but can run continuously (day and night), can be easily transported and set up and present a small field-of-view which removes multiple scattering concerns such as micro-pulse Lidars (MPL) [30] or ceilometers at 1064 nm [31].

The aim of the present work is to evaluate the feasibility of retrieving 1-D aerosol radiative forcing of different types of aerosols from ceilometer signals. It is worth noting that the works commented above are focused on mineral dust; however, this work is focused on the radiative forcing in absence of mineral dust, taking advantage of the exceptional atmospheric situation caused by the appearance of coronavirus SARS-CoV-2 and its associate illness "coronavirus disease 2019" (COVID-19), which has been a great challenge to humankind and its health, environmental, and socio-economic consequences are far to be completely assessed. One of the main exceptional measures to fight against this challenge is the lockdown, imposed in many countries worldwide such as Spain, France, Italy, UK, USA, Argentina, India, Australia, or Ruanda among others, which measures have produced significant social and economic changes. For instance, the lockdown measures have greatly decreased the road traffic and the industrial activity and, therefore, have caused an exceptional situation in the air pollutant emission

scenarios providing a great opportunity to study the impact of these measures on the air composition; the air quality, especially in the most affected urban areas; and evaluate, in terms of power per unit area, the pollutants role in the Earth's radiation budget.

According to [32], the major cities under lockdown measures (e.g., Los Angeles, New York, NY, USA, London, UK, or Mumbai, India) have shown a sharp decrease in gaseous and particle pollution ranging between −9% and −60% compared to data collected during the previous year and between +2% and −55% compared to the 5-year data averaged from 2014 to 2018. In Spain, the lockdown measures were imposed to all non-essential industries and activities by the publication of the 14 March Royal Decree 463/2020, which declared a state of alarm due to the COVID-19 sanitary crisis [33]. Later, these lockdown measures were reinforced by the 27 March Royal Decree 10/2020 [34] and, as a result, a reduction in NO_2 concentrations was observed in Barcelona and Madrid, about 50% and 62%, respectively [35]. Besides, in Barcelona, the authors of [36] showed that the black carbon and O_3 concentrations were reduced by half and PM_{10} decreased but in much lower proportion. Therefore, it can be claimed that the lockdown measures have caused a drastic drop in emissions of many air pollutants.

Then, the radiative forcing estimates from ceilometer signals are used to assess the impact of the lockdown measures on the radiative forcing over Madrid. Besides, as the effect on the radiative budget, and therefore the radiative forcing, of both natural and anthropogenic aerosols still shows large uncertainty [37], the potential results that can be obtained in this study can be highly relevant for air quality and climate change issues. This task was addressed by means of well-known tools as the GAME radiative transfer model and the adaptation to a different wavelength, from 532 to 1064 nm, of the method developed by [10]. The present work uses measurements at 1064 nm from the Lufft CHM15k-Nimbus ceilometer, deployed in the Research Centre for Energy, Environment and Technology (CIEMAT, Madrid, 40.45N; 3.72W), which was continuously measuring during the lockdown. Ceilometer information was thus combined with ancillary satellite and ground-based data to estimate aerosol radiative properties in both SW and LW spectra. Then, different African dust events that impacted the measurement site were identified and used to estimate mineral dust radiative forcing values from ceilometer measurements, which were compared to previous works. Finally, once the methodology was validated, it was applied to the exceptional situation lived in Spain for several months due to the estate of alarm, in order to quantify the radiative consequences of the lockdown measures over Madrid.

The paper is structured as follows. Section 2, "Materials and Methods", includes a brief description of the instrumentation and the dataset used to feed GAME. Section 3, "Results", is devoted to the description of the methodology, its validation by comparison to the literature, and the estimation of the radiative forcing values before and during the lockdown. Section 4, "Discussion", includes an in-depth analysis of the results observed in Section 3. Finally, Section 5 includes a short summary and concluding remarks.

2. Materials and Methods

2.1. Site and Instrumentation

As Figure 1 shows, the monitoring station of the Department of Environment of the CIEMAT (yellow bullet) is located in the center of the Iberian Peninsula (40.45N; 3.72W; 669 m.a.s.l.) in the northwest part of Madrid, a city with a population of about 3.2 million that suffers almost every year from pollution episodes and frequent African dust outbreaks [38]. The Madrid airport (blue bullet), where the radiosondes were launched, and Madrid AERONET station, where the sun-photometer is located (red bullet), are also shown in Figure 1.

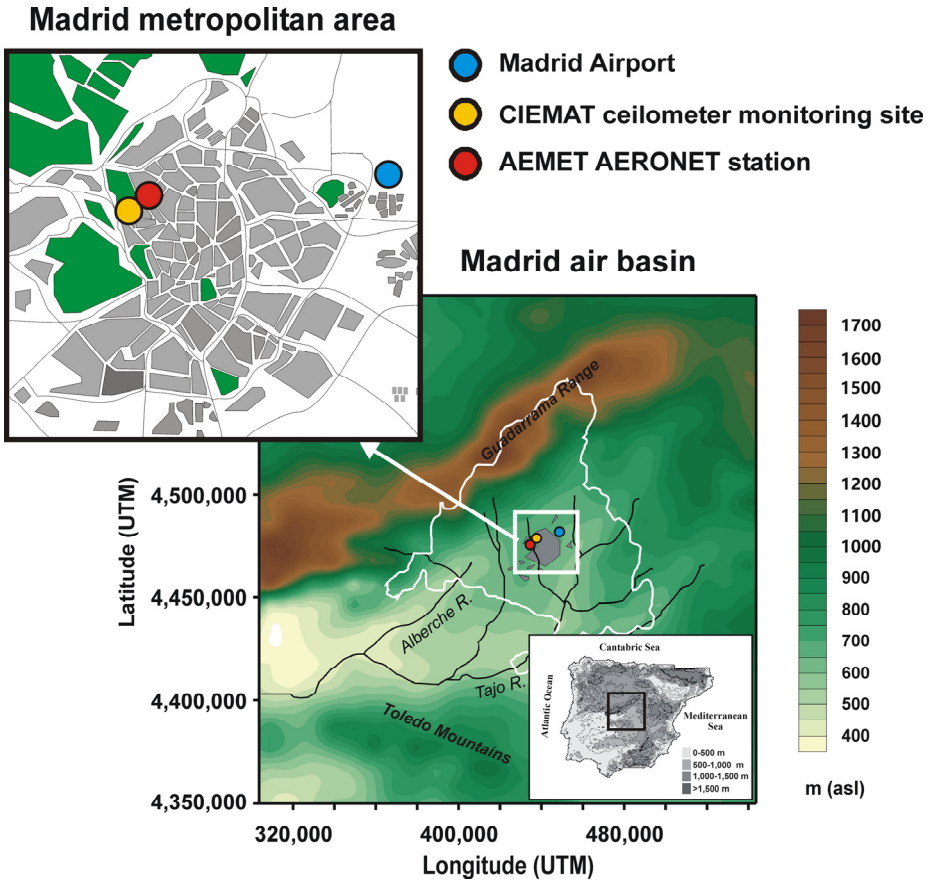

Figure 1. Geographical location of the monitoring site (yellow point), Madrid AERONET station (red point), and the Madrid airport (blue point), where the radiosondes were carried out.

The site has operated a Lufft CHM15k-Nimbus ceilometer [31,39] since December 2019, has an AERONET sun photometer [18], operating since 2012 at the Spanish meteorological agency (AEMET), about 500 m away from the monitoring station, and a co-located multi-wavelength Lidar which belongs to EARLINET [21], included in ACTRIS.

As has been explained in the previous section, the14 March Royal Decree 463/2020 declared a state of alarm due to the COVID-19 sanitary crisis, the so-called lockdown period, and introduced restrictions to mobility, i.e., people only could circulate through a public road individually to do the groceries, go to the doctor, or the office or other acts of force majeure. Transports and all non-essential industries and activities such as visiting sports venues, museums, libraries, and other cultural places or bars and restaurants were also significantly reduced or even forbidden [33].

Then these restrictions were reinforced by the 27 March Royal Decree 10/2020 [34], total lockdown period. The latter took place between 28 March and 9 April and limit some industries classified as essential, for instance the construction sector that remained operating after the 14 March Royal Decree 463/2020 was limited during those 10 days, and just the vital sectors as food industry remained operating during the total lockdown period, causing a remarkable change in the aerosol optical properties (see Section 3.2).

2.2. CHM15k-Nimbus Ceilometer

The ceilometer CHM15k-Nimbus operates with a pulsed Nd: YAG laser emitting at 1064 nm. According to the manufacturer, the output power per pulse is 59.5 mW with a repetition frequency ranging between 5 and 7 kHz. The temporal resolution is 15 s and the vertical resolution is 15 m, with the maximum height being 15,360 m.a.g.l. The field of view of the telescope that collects the laser

backscattered signal is 0.45 mrad and the laser beam divergence is less than 0.3 mrad. At the end of the optical chain, after the telescope an avalanche photodiode in photon-counting mode detects the backscattered signal. According to the manufacturer, the overlap of the telescope and the laser beam is 90% complete between 555 and 885 m.a.g.l., and according to the work in [31], the complete overlap is found about 1500 m above the instrument.

Retrieval of Ceilometer Backscattering Coefficient Profile

Following the methodology presented in [39], the attenuated backscatter obtained from the ceilometer signals is used to estimate the backscattering coefficient that allows monitoring and comparing singular events. As the authors of [39] show, it is possible to apply the Klett–Fernald inversion [40–43] to ceilometer data, by manually selecting the necessary reference height (Z_{ref}). The presence of a multi-wavelength Raman lidar, belonging to EARLINET, co-located with the ceilometer is leveraged to quantify the differences between the ceilometer backscattering coefficient inversions and the inversions calculated independently with the Raman lidar.

A total of 6 measurements, summarized in Table 1, performed by the multi-wavelength lidar are analyzed. These measurements present different temporal averaging, from 20 to 90 min in different days in order to estimate particle backscatter coefficients in different atmospheric situations. Elastic inversions using the Klett–Fernald method are applied to the averaged profiles at 1064 nm using a fixed Lidar ratio of 50 sr. The spatial resolution of the multi-wavelength Lidar (3.75 m) has been downscaled to 15 m for the comparison with the ceilometer. The elastic inversion following the Klett–Fernald method is applied to the same 6 selected periods. In both systems, the Z_{ref} is selected manually.

Table 1. Characteristics and statistical parameters of the 6 cases.

Case #	Day	Hour (UTC)	*NMB* [%]	*R*
1	14-07-2020	16:30–17:27	4.59	0.9930
2	14-07-2020	20:30–21:31	15.68	0.9866
3	15-07-2020	14:00–15:01	13.80	0.9975
4	15-07-2020	18:00–19:01	2.17	0.9955
5	20-07-2020	15:17–15:39	2.55	0.9964
6	20-07-2020	20:01–20:30	0.17	0.9894

As in [39], the quality of the inversions of the 6 studied cases is determined by two statistical parameters that measure the agreement between the ceilometer and lidar backscatter coefficients, the first one is the normalized mean bias (*NMB*),

$$NMB\ [\%] = \frac{\left|\overline{\beta}_{ceil} - \overline{\beta}_{lidar}\right|}{\overline{\beta}_{lidar}} * 100 \quad (1)$$

where $\overline{\beta}_{ceil}$ and $\overline{\beta}_{lidar}$ represent the mean particle backscatter coefficients estimated from ceilometer and Lidar signals, respectively. The second statistical parameter is the correlation coefficient (R) of the profiles. Both statistical parameters for the 6 cases can be found in Table 1. The threshold selected for the two statistical parameters in order to determine if the inversions present a good quality were defined in [39]: $NMB < 15\%$ and $R > 0.92$.

Therefore, it can be inferred that 5 cases (cases 1, 3, 4, 5, and 6) present a good quality inversion and only one case does not fulfill the criteria. Figure 2 shows the 6 cases; the blue lines correspond to the 5 cases that fulfill both criteria while case 2 is shown in red.

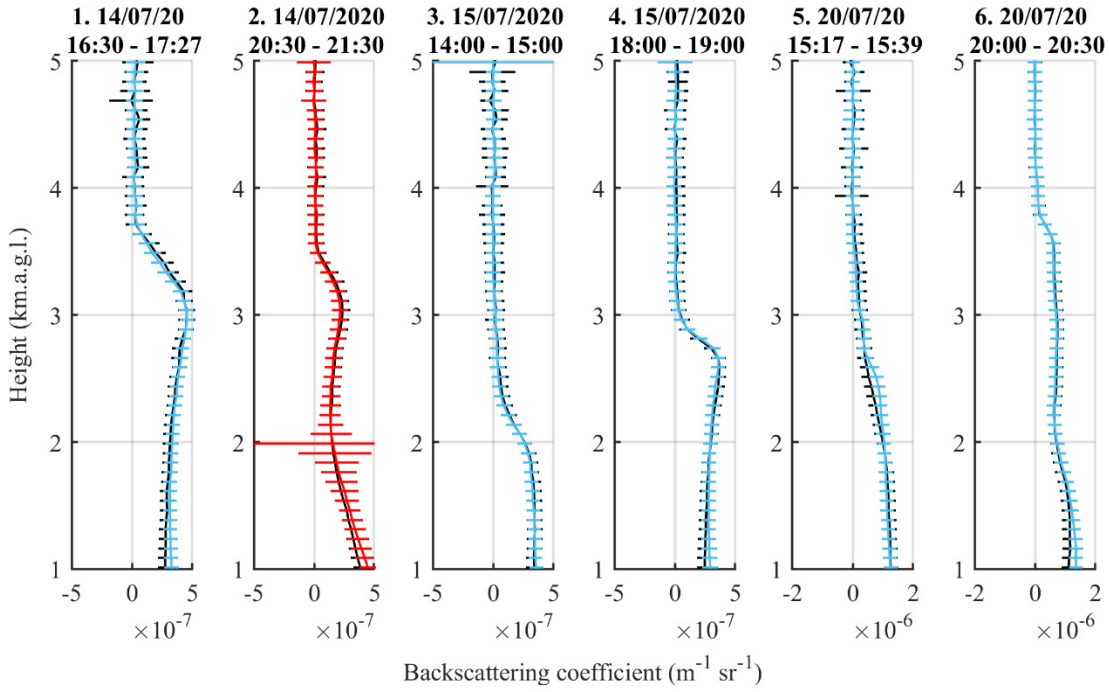

Figure 2. Lidar (red and blue lines) and ceilometer (black lines) backscattering coefficient profiles for the 6 cases detailed above. The case marked in red do not fulfill the *NMB* and *R* criteria. Errors bars in Lidar and ceilometer profiles have been estimated using the Monte Carlo method [21].

The first kilometer is not shown in Figure 2 due to the overlap effect explained above. Case 2 presents huge error values at 2 km, probably caused by the presence of clouds during the measurement, which are responsible of the high *NMB* value (15.68%).

Once has been demonstrated that the ceilometer signals are equivalent to the Lidar signals at 1064 nm, previous ceilometer signals are used to study the evolution of radiative forcing values during the COVID-19 lockdown by means of the GAME radiative transfer model.

2.3. AERONET Sun Photometer

AERONET is a network that, by means of worldwide deployed automated sun and lunar photometers, the latter of which used for nighttime operation, provides worldwide observation of aerosol optical, microphysical, and radiative properties. The sun photometers, that are described in detail in [18], are robotically pointed sun/sky spectral radiometers named CIMEL CE 318 photometer, which principally measures direct solar irradiances and sky radiances (in the almucantar and principal plane scenarios) at several wavelengths that are between 340 and 1020 nm. The main product provided by AERONET is the aerosol optical depth (AOD) that according to [44] presents a wavelength-dependent accuracy at overhead sun and assuming an air mass value equal to 1, thus in the UV band presents the minimum accuracy with a root mean square error about ±0.012 while in the IR band the AOD presents the minimum root mean square error (±0.006). Several products are retrieved from the AOD and sky radiances values, using an algorithm described in [19,45]. The most important AOD-derived products for radiative forcing calculations and therefore for this work are the columnar particle size distribution, asymmetry factor (*asy*), and single scattering albedo (SSA). Besides, these works also detail the errors associated to the retrieval of these AOD-derived products, thus in the case of the particle size distribution, for particles whose radius falls between 0.1 and 7 μm the error in the retrievals are around 10 and 35%, whereas for radii below 0.1 or above 7 μm the retrieval errors increase to values around 80 and 100%. The error associated to the retrieval of SSA, which is about ±0.03 for AOD values greater than 0.4 (considered as high aerosol load) and solar zenith angle (θ_z) greater than 50° and ±0.02 for AOD lower than 0.2 (considered as low aerosol load). At the moment this work

was performed, Level 2.0 AERONET sun photometer data were not available and therefore Version 3 Level 1.5 AERONET sun photometer data is used to determine the columnar aerosol properties. Due to the use of Level 1.5 AERONET data, some uncertainties associated to the estimation of the SSA can be propagated to the radiative forcing estimates. In order to give light to those uncertainties, a perturbation analysis has been performed showing that small variations in the SSA lead to variations in the radiative forcing values, therefore the individual values must be analyzed carefully.

2.4. EARLINET Lidar

At the CIEMAT site (Madrid), a ground-based Raman Lidar station belonging to EARLINET is in regular operation. The characteristics of EARLINET, its main goal, and the required set-up to be part of the network can be found in [21]. The Lidar system is a laboratory equipment based on a Nd:YAG pulsed laser source (Spectra Physics LAB170-30) emitting the fundamental (1064 nm), 2nd, and third harmonics (532 and 355 nm) at 30 Hz and a 30 cm diameter Newtonian telescope, which acts as a light receiver and a detection block including a photon-counting acquisition system. The instrument is operated vertically due to safety reasons. Other instrument characteristics have been described elsewhere [46]. Lidar signals are recorded with 1-min resolution (1800 laser pulses), but later 30 to 60 min files are averaged in order to derive vertically-resolved aerosol extinction coefficient profiles with signal-to-noise ratio values larger than 3 up to the tropopause. The noise component is estimated from altitudes between 25 and 30 km, where the laser light contribution can be considered negligible. In the present work, only the elastic channel at 1064 nm is employed to derive vertical profiles by means of the Klett–Fernald algorithm [40–43] using an aerosol extinction-to-backscatter ratio of 50 sr, typical for continental aerosol. The Rayleigh extinction coefficient has been calculated based on the revision of the theory [47] using vertical profiles of meteorological data from the AEMET radiosonde station at the Barajas airport, located 15 km away from the measurement site.

2.5. GAME Main Features and Input Parameters

The GAME code, which has satisfactorily demonstrated its capabilities to estimate the aerosol radiative forcing in previous works such as, e.g., in [1,9,10,16], is widely described in [7,8] and its LW part in [2]. This model is used in the present work to simulate SW and LW radiative fluxes with and without aerosols and, hence, to estimate the radiative forcing at the bottom of the atmosphere (BOA) and at the top of the atmosphere (TOA) during the COVID-19 lockdown in Spain. The radiative forcing is defined as the change in the radiation levels due to the atmospheric aerosols:

$$RF_{BOA} = \left(F_{BOA}^{DN} - F_{BOA}^{UP}\right) - \left(F_{BOA}^{DN,0} - F_{BOA}^{UP,0}\right) \quad (2)$$

$$RF_{TOA} = \left(F_{TOA}^{DN} - F_{TOA}^{UP}\right) - \left(F_{TOA}^{DN,0} - F_{TOA}^{UP,0}\right);\ RF_{TOA} = F_{TOA}^{UP,0} - F_{TOA}^{UP} \quad (3)$$

where F stands for radiative flux, the superscripts DN and UP indicate whether the fluxes are downward or upward, respectively, and 0 points out the radiative fluxes without aerosols. The simplification of Equation (3) implies that the amount of the incoming solar radiation is equal with and without aerosols at the TOA.

It is worth to note that LW fluxes are often neglected in regional and global climate models [2], but [2,9,10] show that the LW component of the radiative forcing represents between 20% and 25% of the SW radiative forcing, pointing out that both spectral ranges must be considered to avoid overestimations on mineral dust cooling effect. The SW and LW fluxes are estimated in two adjustable spectral ranges using the discrete ordinates method [48] at the boundaries of plane and homogenous atmospheric layers. Thus, in this work the SW spectral range is set between 0.3 and 4 μm and the LW spectral range is set between 4 and 37 μm. Besides, GAME presents a variable spectral sampling, depending on the spectral range considered and the wave number in the SW spectral range. On the other hand, the LW spectral range presents a fixed spectral sampling of 115 values.

GAME presents a variable spatial resolution, thus the LW part of the code is divided into 40 vertical levels between ground and 100 km height: 1km from the surface to 25 km height, 2.5 km between 25 and 50 km, 5 km from 50 to 60 km, and 20 km between 80 and 100 km. The SW version is divided into 18 vertical levels between ground and 20 km height with a resolution of 5m from the surface to 10 m, 10 m between 10 and 50 m, 50 m between 50 and 100 m, 100 m between 100 and 200 m, 1 km between 1 and 2 km, 2 km between 2 and 10 km, and 10 km between 10 and 20 km.

Table 2 lists the main parameters used as inputs of GAME in the SW and LW spectral range; it is worth noting that some of these characteristics can be tuned depending on the type and the characteristics of the research carried out. Thus, in order to retrieve the radiative forcing, GAME is firstly fed by the vertical distribution of aerosols, which is obtained from ground-based extinction profiles (see Section 2.1) calculated from the CHM15K-Nimbus ceilometer backscattering coefficient at 1064 nm (β_{1064}). Then, SSA, asymmetry factor (*asy*), and particle size distribution from AERONET are also used as inputs. Finally, GAME is also fed with meteorological profiles including vertically resolved temperature, pressure, relative humidity, air density, and O_3 concentration retrieved from radiosonde data. The radiosondes are launched at 00 and 12 UTC every day from the Madrid-Barajas station, which is located about 15 km away from the measurement site.

This dataset composed by extinction profiles, AERONET, and radiosonde data has been validated in the literature [1,9,16,49]. The extinction coefficient profiles and AOD considered in the study are assumed to be due to the mineral dust particles in the validation section and due to a mix of local natural and anthropogenic aerosol during the COVID-19 lockdown. The satellite data are taken from COPERNICUS Global Land Services, which uses a constellation of geostationary satellites (Meteosat Second Generation, GOES, MTSAT/Himawari) and provide hourly data. Measures of land surface temperature (ST) and surface albedo close to the selected time for the averaged ceilometer measurements are chosen. The time-dependent or imaginary part of the refractive indices used for the SW calculations are taken from AERONET sun photometer measurements while the time-independent or real part of the refractive indices used in this study for the LW spectral range are taken from in [50].

Table 2. Input parameters for the GAME model and data sources in the SW and LW spectral ranges. Note that the sources of the input and some parameters can be adjusted depending on the characteristics of the research.

Parameters		Shortwave	Longwave
Spectral range (adjustable)		0.3–4 µm	4–50 µm
Number of sub-bands (non-adjustable)		167	115
Atmospheric parameters (different sources)	Atmospheric profile	Radio soundings	Radio soundings
	H_2O	Radio soundings	Radio soundings
	O_3 profile	U.S. standard atmosphere	U.S. standard atmosphere
	Absorption coefficients of main gases	HITRAN	HITRAN
	Surface albedo	COPERNICUS Global land service	-
	LW emissivity	-	CERES
Meteo parameters (different sources)	At surface	COPERNICUS Global land service	
	<20 km	Radio soundings	
	>20 km	U.S. standard atmosphere	
Aerosols (different sources)	AOD	Ceilometer extinction coefficient, AERONET	Mie calculation
	Single-scattering albedo	AERONET	Mie calculation
	Asymmetry factor	AERONET	Mie calculation
	Aerosol vertical distribution	Ceilometer signal	Ceilometer signal
	Size distribution	-	AERONET
	Fine and coarse mode radius	-	AERONET
	Fine and coarse mode concentration	-	AERONET
	Refractive index	-	Krekov [50]

3. Results

3.1. Comparison of the Aerosol Radiative Forcing Estimates with Previous Studies

Before the estimation of the radiative forcing due to aerosols, dust radiative properties in the SW and LW spectra are estimated and compared with mineral dust radiative forcing values from previous works in order to validate the methodology and, therefore, the estimated radiative forcing values. The need for this evaluation is given by the fact that the significant researches in the literature that used GAME, for instance, in [2,9–11,14,49,51] among others, are mainly focused in the study of African dust outbreaks. Mineral dust is frequently injected from desert regions of North Africa into the atmosphere through resuspension processes and then carried, at different altitudes, across the Mediterranean basin to Europe [52]. According to the work in [53], central Spain is affected by mineral dust events most frequently during summer but also during winter, though more sporadically.

The criterion followed to identify dusty days over the study site is the one used since 2004 by the Spanish and Portuguese governments. This is one of the official methods recommended by the European Commission to detect and identify African dust episodes [54] and its soundness has been demonstrated in the literature [55–58]. The methodology, widely described in [58], is based on the interpretation and daily consultation of data retrieved from multiple sources as back-trajectories computed by the HYSPLIT (Hybrid Singles Particle Lagrangian Integrated Trajectory Model) [59] model, satellite image, synoptic meteorological charts, and different dust forecast models, namely, SKIRON (University of Athens, https://forecast.uoa.gr/en/forecast-maps/dust/europe), NMMB/BSC along with BSC-DREAM8b v2.0 (Barcelona Supercomputing Center, http://www.bsc.es/projects/earthscience/DREAM/) and NAAPS (Naval Research Laboratory in Monterey (CA), https://www.nrlmry.navy.mil/aerosol/).

In this study, eight cases were selected and analyzed, for which back-trajectories and products from dust forecast models indicated the presence of African dust over the center of the Iberian Peninsula. Thus, the radiative forcing values for the different eight cases are given in Table 3. A negative or positive sign of the aerosol radiative forcing determines whether the aerosols produce a cooling or a heating effect [60].

Table 3. Mineral dust radiative forcing (RF, last four columns), at the surface (BOA), and the top of the atmosphere (TOA) for the LW and SW, estimated for the 8 African dust events. Time refers to the ceilometer start time (all ceilometer measurements are of 1 h duration). AOD, SSA (single scattering albedo), and *asy* (asymmetry factor) are measured by the AERONET sun photometer at 440 nm. θ_z stands for the solar zenith angle in degrees. Surface albedo, taken from COPERNICUS Global Land Services, is 0.013 for every case. ST is the surface temperature taken from COPERNICUS Global Land Services. Fine-mode-fraction is shown together with its standard deviation, provided by AERONET. The letter "d" in the case number denotes that these 9 cases are affected by mineral dust.

Case	Day	Time (UTC)	θ_z [°]	AOD_{440}	SSA_{440}	asy_{440}	Fine-Mode-Fraction	ST [K]	RF [W m^{-2}]			
									SW BOA	SW TOA	LW BOA	LW TOA
1d	04-02-2020	16:31	79.53	0.18	0.71	0.73	0.59 ± 0.09	287.07	−25.39	−8.45	+5.47	+1.46
2d	07-02-2020	16:26	78.02	0.33	0.91	0.76	0.56 ± 0.11	283.34	−32.71	−22.49	+7.98	+3.68
3d	28-02-2020	8:33	83.38	0.24	0.95	0.74	0.23 ± 0.09	274.55	−19.89	−12.64	+11.98	+3.44
4d	19-03-2020	11:50	41.75	0.70	0.94	0.77	0.24 ± 0.12	290.85	−66.39	−46.72	+3.84	+3.30
5d	24-03-2020	6:26	87.77	0.18	0.97	0.73	0.55 ± 0.12	286.67	−1.31	−2.68	+5.27	+2.75
6d	29-03-2020	8:11	78.21	0.13	0.93	0.72	0.80 ± 0.16	280.47	−13.65	−9.10	+1.17	+0.43
7d	08-05-2020	8:35	63.48	0.19	0.93	0.71	0.53 ± 0.09	295.37	−24.69	−13.62	+6.24	+1.69
8d	08-05-2020	17:14	67.66	0.19	0.93	0.68	0.57 ± 0.08	300.11	−24.19	−13.68	+7.02	+2.51

Figure 3 is composed of maps from BSC-DREAM8b v2.0 (Figure 3a), NMMB/BSC (Figure 3b), NAAPS (Figure 3c), and SKIRON (Figure 3d) dust forecast models, for one of the cases presented in Table 3, concretely the case 3d (28 February). Green (Figure 3a–c) and brown (Figure 3d) areas confirm the presence of mineral dust over the Iberian Peninsula, and therefore over the measurement

site, during the chosen day. The good agreement obtained among the maps provided by the different models confirms that this day can be classified as dusty day.

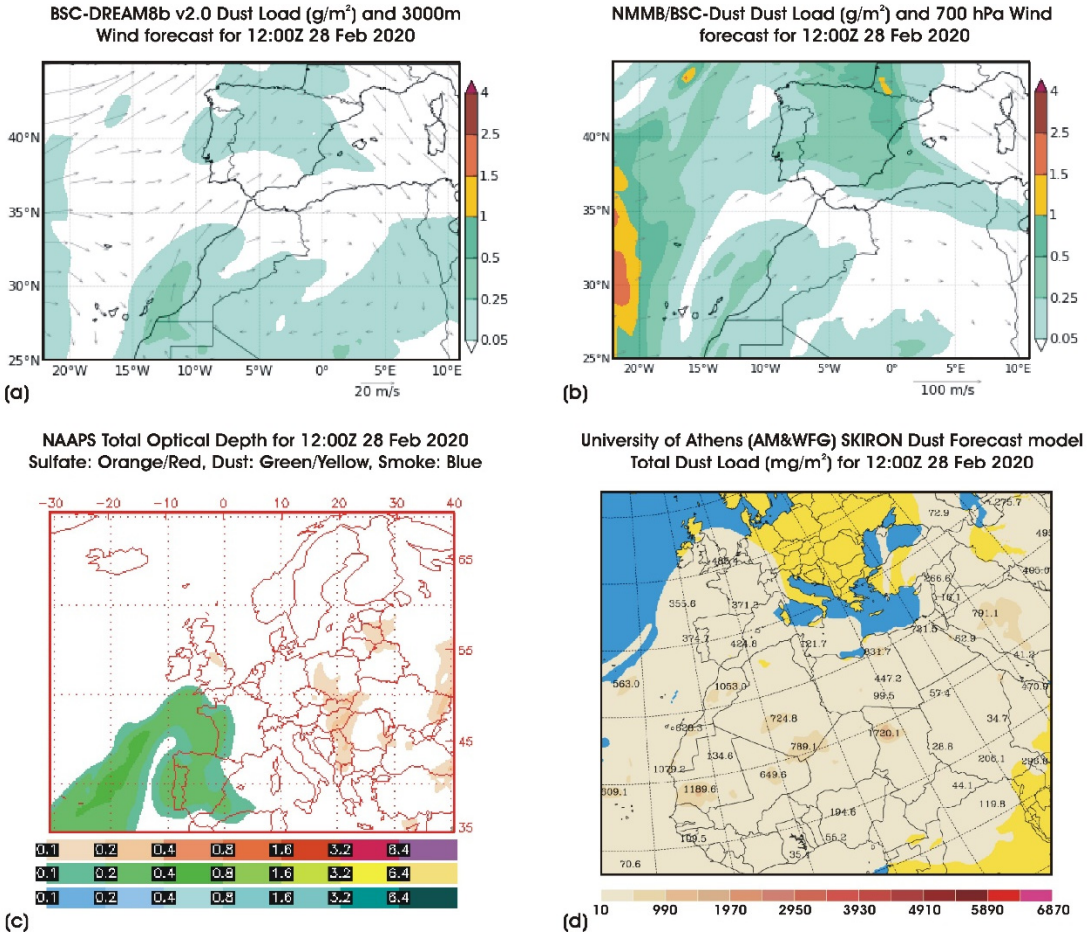

Figure 3. Maps of total dust load (**a**,**b**,**d**) and optical depth values (**c**) over the Iberian Peninsula predicted for 28 February by the BSC-DREAM8b v2.0 (**a**), NMMB/BSC (**b**), NAAPS (**c**), and SKIRON (**d**) dust models. Colored areas (**a**–**c**) and brown areas (**d**) point out the presence of mineral dust in the atmosphere. Arrows in panels (**a**,**b**) stand for wind direction.

In the SW spectral range, the radiative forcing estimates present a cooling effect (values ranging between −1.31 and −66.39 W m^{-2} at BOA and between −2.68 and −46.72 W m^{-2} at TOA), while in the LW spectral range, they present a heating effect (values ranging between +1.17 and +11.98 W m^{-2} at BOA and between +0.43 and +3.68 W m^{-2} at TOA), being, in general, the heating effect in the case of the LW spectral range lower than the cooling effect of the SW.

The range of values of the SW radiative forcing is consistent with forcing measurements made in Madrid [58], other locations as Granada [1], Barcelona [2], Southwestern Spain [61], Italy [16], and central Europe [10]. For instance, the authors of [58] found values at the surface ranging between −15 and −60 W m^{-2} and between −1 and −40 W m^{-2} at TOA, depending on the aerosol load. The authors of [2] found values of −55.4 W m^{-2} and −22.8 W m^{-2} at the BOA and at the TOA respectively for AOD_{500} = 0.38, while for AOD_{500} = 0.17 found −24.4 W m^{-2} at the BOA and −6.6 W m^{-2} at the TOA. In the present work, case 4d presents the highest AOD_{440} (0.70) and the highest, in absolute terms, radiative forcing at the SW (−66.39 W m^{-2} and −46.72 W m^{-2} at the BOA and the TOA respectively), while case 1d presents, with a low AOD_{440} value (0.18), radiative forcing values about −25.39 W m^{-2} at the BOA and −8.45 W m^{-2} at the TOA. Therefore, the radiative forcing in the SW is directly related with the aerosol load; that is, the bigger the AOD, the greater the cooling effect.

In the LW spectral range the radiative forcing estimated values are consistent with the values found in previous works as [62,63] and some of the works commented above [1,2,9,10,16]. In the present work, the LW radiative forcing represents around 22% of the SW at the BOA and around 12% at the TOA, except in case 5d because of its high solar zenith angle. These percentages are in agreement with the differences between the SW and LW components found in [9], where the LW contribution is less than 25% than the SW one.

It is worth noting that, because of the solar zenith angle, cases 3d (θ_z = 83.38º) and 5d (θ_z = 87.77º) break the previous rules; therefore, comparing case 5d to case 6d, a case with a lower solar zenith angle (θ_z = 78.21º) and AOD_{440} (0.13) 28.18% lower, in the SW at the surface (BOA) the cooling effect of case 5d (−1.31 W m^{-2}) is 90.40% lower than the one of case 6d (−13.65 W m^{-2}). At the TOA the difference is about 70.55% between both cases (−2.68 and −9.10 W m^{-2}). Case 3d presents a similar behavior if it is compared to case 7d, a case with a lower solar zenith angle (θ_z = 63.48º), that is, the AOD_{440} of case 3d is about 0.24, a 17.52% greater than the AOD_{440} of case 7d (0.19). In spite of this difference, the cooling effect at the BOA for case 3d is about −19.89 W m^{-2} and at the TOA is −12.64 W m^{-2}, while for case 7d, the cooling effect at the BOA and at the TOA is about −24.69 W m^{-2} (24.13% greater than case 3d) and −13.62 W m^{-2} (7.75% greater), respectively. Therefore, during the first or last hours of the day when the solar zenith angle is close to 90º (low solar incoming radiation), the cooling effect of the aerosols is much lower in spite of the high AOD. The LW radiative forcing also presents a greater impact on the Earth radiative budget than the SW radiative forcing. For instance, in the study of [2] low radiative forcing values were found in cases of high AOD associated with large solar zenith angles.

3.2. Aerosols Radiative Forcing

3.2.1. AERONET AOD at 440 nm Temporal Evolution

Figure 4 shows the temporal evolution of the AERONET AOD at 440 nm (level 1.5 data) weekly mean values for the period between 27 January and 15 June and the 6-year weekly AERONET AOD_{440} average for the period 2014 to 2019 in the same dates, for Madrid AERONET station. In this figure, the time series of the AOD_{440} for the year 2020 are also included. For this year, the lockdown period that began during week 11th (14 March) is marked in pink color. The beginning of the lockdown matched with a Saharan dust event (in yellow), which causes a strong peak in the 2020 AOD_{440} (about 0.63), while for the period 2014–2019 the AOD_{440} is much lower (about 0.03). Before the total lockdown (between 27 March and 9 April, marked in green), the AOD_{440} of both time periods, 2014–2019 and 2020, match until week 15th, pointing out that the Saharan dust event that affects the 2020 data, is not affecting anymore the optical properties. After that, the AOD_{440} values for the period 2014–2019 increase until week 17th from 0.14 to 0.19, while in 2020 the AOD_{440} decreases since week 15th from 0.14 to 0.08 in week 17th. The latter is the minimum AOD_{440} value found during the lockdown. This decrease evidences the effect of the total lockdown period, showing in turn that the lockdown had a clear effect on the aerosol loading. As has been shown above, a direct relation between AOD and radiative forcing exists; therefore, the observed variation in the AOD_{440} due to the COVID-19 lockdown should have an effect in the radiative forcing that can be studied by means of the radiative transfer model GAME.

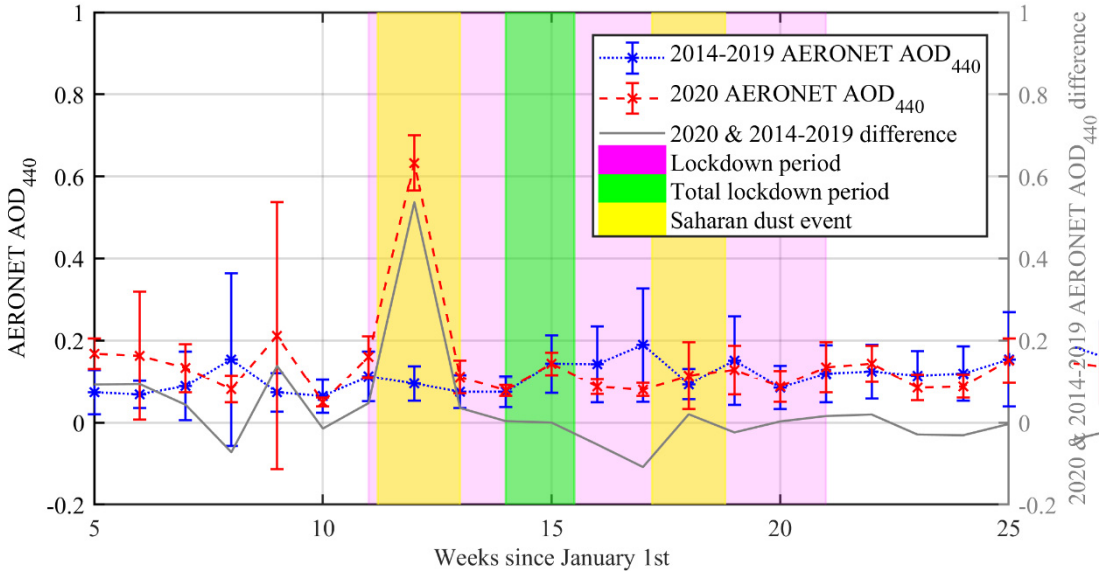

Figure 4. AERONET AOD at 440 nm temporal evolution. Blue line stands for 6-year weekly AERONET AOD_{440} average (from 2014 to 2019). Red line stands for AERONET AOD_{440} weekly mean values in 2020. Gray line represents the difference between both lines; negative values point out lower AOD_{440} during 2020 compared to AOD_{440} values found in previous years. Colored areas stand for Saharan dust events, lockdown period and total lockdown period during 2020 in yellow, pink and green, respectively. Errors have been estimated using standard deviation. Only Saharan dust outbreaks during the lockdown period are shown.

3.2.2. Aerosol Radiative Forcing

Specific ceilometer measures from January to May were selected to estimate the aerosol radiative forcing due to anthropogenic activity in Madrid before and during the estate of alarm. Measures obtained after 8 UTC in the morning were analyzed to assess the effect of the road traffic during the very first hours of the workdays. Additionally, measures carried out in the afternoon after 16 UTC were obtained to assess the radiative effect of all the industrial activity and the road traffic emissions accumulated along the day.

In Tables 4 and 5, the aerosol radiative forcing estimates, excluding mineral dust intrusions, are presented for 18 and 19 different cases in the morning and in the afternoon respectively. In both tables, the first 12 cases correspond to radiative forcing estimated before the lockdown, while the remaining cases correspond to the radiative forcing estimated in the lockdown period. As for the radiative forcing induced by mineral dust, all the cases present a cooling effect both at the TOA and at the BOA in the SW spectral range while in the LW a heating effect is observed. The authors of [58], in agreement with the results of this research, found at the BOA and at the TOA in the absence of mineral dust a cooling effect in the SW spectral range in the same region of study. These authors, who found at the surface values ranging between −15 and −75 W W m^{-2} and at the TOA between −1 and −35 W m^{-2}, show that the radiative forcing at TOA presents a lower cooling effect than at the BOA in the absence of mineral dust. In the present work, in the SW, the aerosol radiative forcing ranges between −6.85 and −15.80 W m^{-2} in the morning and between −0.33 and −24.01 W m^{-2} in the afternoon at the BOA and ranges between −1.25 and −6.87 W m^{-2} in the morning and between −0.37 and −11.69 W m^{-2} in the afternoon at the TOA. Therefore, as in the work in [58], the cooling effect at the BOA is greater than at the TOA. In the LW the heating effect at the BOA (values ranging between +0.55 and +3.06 W m^{-2} for the morning cases and between +0.06 and +3.99 W m^{-2} for the afternoon cases) is also greater than the heating effect at the TOA (values ranging between +0.04 and +0.96 W m^{-2} for the morning case and +0.02 and +1.32 W m^{-2} for the afternoon cases) as in the 9 cases with mineral dust.

Table 4. Aerosol radiative forcing (last four columns), estimated for 28 different mornings without presence of mineral dust in the atmosphere, at the BOA and the TOA for the LW and SW. Time refers to the ceilometer start time (all ceilometer measurements are of a duration of 2 h). Fine-mode-fraction is shown together with its standard deviation, provided by AERONET. The letter "m" in the case number denotes that these are morning cases. Radiative forcing estimates considered as outliers by the boxplots (see Figures 5 and 6) are marked in bold.

Case	Day	Time (UTC)	θ_z [°]	AOD_{440}	SSA_{440}	asy_{440}	Fine- Mode-Fraction	ST [K]	RF [W m^{-2}]			
									SW BOA	SW TOA	LW BOA	LW TOA
1m	08-01-2020	8:30	82.95	0.09	0.90	0.81	0.61 ± 0.13	271.97	−8.98	−6.87	+0.55	+0.04
2m	09-01-2020	8:22	84.11	0.09	0.77	0.71	0.87 ± 0.17	274.96	−8.83	−2.49	+1.47	+0.04
3m	14-01-2020	8:20	84.13	0.19	0.84	0.71	0.88 ± 0.17	270.77	−15.80	−6.49	+0.77	+0.06
4m	18-02-2020	9:06	70.59	0.07	0.89	0.76	0.88 ± 0.27	275.44	−10.18	−3.95	+1.27	+0.23
5m	19-02-2020	8:30	76.04	0.08	0.89	0.72	0.84 ± 0.19	277.30	−10.98	−4.85	+2.12	+0.33
6m	20-02-2020	8:27	76.27	0.08	0.81	0.72	0.82 ± 0.18	276.23	−12.43	−3.72	+1.71	+0.15
7m	21-02-2020	8:32	75.16	0.06	0.74	0.74	0.77 ± 0.16	277.66	−11.15	−1.80	+2.48	+0.31
8m	22-02-2020	8:33	74.70	0.06	0.81	0.71	0.84 ± 0.19	277.81	−9.54	−3.00	+0.69	+0.06
9m	23-02-2020	8:28	75.25	0.04	0.84	0.74	0.78 ± 0.18	279.15	−6.85	−2.41	+0.80	+0.06
10m	26-02-2020	8:33	73.53	0.05	0.92	0.70	0.41 ± 0.12	278.82	−8.66	−4.10	+1.83	+0.45
11m	02-03-2020	8:57	68.02	0.05	0.80	0.74	0.83 ± 0.46	282.25	−10.21	−1.25	+3.06	**+0.96**
12m	11-03-2020	8:18	71.69	0.08	0.79	0.71	0.59 ± 0.09	283.89	−14.64	−2.52	+1.02	+0.35
13m	26-03-2020	8:22	66.06	0.06	0.86	0.73	0.66 ± 0.15	282.21	−9.59	−2.64	+0.87	+0.37
14m	20-04-2020	8:37	55.81	0.08	0.92	0.70	0.80 ± 0.13	284.73	−9.12	**−4.11**	+0.70	+0.28
15m	29-04-2020	8:20	56.77	0.07	0.91	0.72	0.60 ± 0.13	287.96	−9.11	−2.62	+0.36	+0.15
16m	18-05-2020	8:32	51.24	0.05	0.88	0.69	0.63 ± 0.08	293.93	−7.46	−1.75	+0.96	+0.19
17m	19-05-2020	8:25	52.45	0.06	0.87	0.69	0.63 ± 0.09	295.63	−8.20	−1.97	+1.29	+0.71
18m	20-05-2020	8:27	51.95	0.06	0.88	0.69	0.61 ± 0.09	297.88	−8.43	−1.92	**+3.64**	+1.28

Table 5. Aerosol radiative forcing (last four columns), estimated for 30 different afternoons without presence of mineral dust in the atmosphere, at the BOA and the TOA for the LW and SW. Time refers to the ceilometer start time (all ceilometer measurements are of a duration of 2 h). Fine-mode-fraction is shown together with its standard deviation, provided by AERONET. The letter "a" in the case number denotes that these are afternoon cases. Radiative forcing estimates considered as outliers by the boxplots (see Figures 5 and 6) are marked in bold.

Case	Day	Time (UTC)	θ_z [°]	AOD_{440}	SSA_{440}	asy_{440}	Fine- Mode-Fraction	ST [K]	RF [W m^{-2}]			
									SW BOA	SW TOA	LW BOA	LW TOA
1a	08-01-2020	16:38	86.14	0.07	0.92	0.55	0.61 ± 0.01	279.70	−5.27	−4.14	+0.61	+0.11
2a	09-01-2020	16:20	83.26	0.15	0.80	0.55	0.74 ± 0.12	278.87	−13.83	−5.44	+1.30	+0.12
3a	14-02-2020	16:33	77.45	0.23	0.87	0.63	0.75 ± 0.13	284.65	−24.01	**−11.69**	+3.99	+0.99
4a	15-02-2020	16:26	76.07	0.15	0.93	0.53	0.74 ± 0.15	287.14	−16.98	**−11.36**	+0.06	+0.02
5a	16-02-2020	16:21	75.01	0.07	0.90	0.63	0.80 ± 0.14	288.08	−9.82	−4.42	+1.29	+0.35
6a	19-02-2020	16:26	75.08	0.07	0.86	0.53	0.64 ± 0.09	285.41	−10.54	−4.98	+2.24	+0.66
7a	20-02-2020	16:26	74.83	0.12	0.75	0.65	0.79 ± 0.14	287.17	−19.03	−4.29	+3.68	+1.06
8a	21-02-2020	16:41	77.09	0.08	0.68	0.65	0.68 ± 0.09	288.25	−13.16	−2.51	+1.53	+0.46
9a	22-02-2020	16:29	74.83	0.07	0.80	0.65	0.73 ± 0.11	289.56	−11.67	−3.68	+3.46	+0.94
10a	26-02-2020	17:03	79.69	0.03	0.83	0.66	0.60 ± 0.12	288.61	−5.67	−1.78	+2.43	+0.81
11a	02-03-2020	18:33	88.68	0.05	0.96	0.55	0.88 ± 0.65	282.25	−0.33	−0.37	+2.48	+0.67
12a	11-03-2020	16:11	67.38	0.11	0.79	0.53	0.33 ± 0.06	297.80	−20.84	−4.33	+2.84	+1.32
13a	01-04-2020	17:05	72.50	0.10	0.86	0.66	0.91 ± 0.22	287.19	**−16.80**	−4.38	+0.78	+0.30
14a	29-04-2020	16:24	59.67	0.09	0.97	0.55	0.60 ± 0.13	317.00	−11.97	−8.97	+0.92	+0.78
15a	10-05-2020	17:26	69.61	0.06	0.96	0.66	0.68 ± 0.14	294.11	−7.64	−4.52	+2.81	+1.32
16a	17-05-2020	16:18	55.76	0.09	0.97	0.57	0.62 ± 0.09	298.74	−9.89	−6.05	+2.58	+1.59
17a	18-05-2020	16:30	57.89	0.07	0.90	0.60	0.61 ± 0.07	302.54	−10.23	−3.78	+6.24	+2.94
18a	19-05-2020	16:27	57.19	0.06	0.89	0.54	0.65 ± 0.08	305.40	−8.01	−3.24	+4.39	+2.20
19a	20-05-2020	16:29	57.44	0.06	0.81	0.60	0.57 ± 0.07	305.74	−9.18	−2.39	+4.88	+2.26

4. Discussion

The heating and cooling effect clearly show the consequences that the presence of mineral dust has on the atmosphere: the mean radiative forcing values and their standard deviation found with mineral dust are about −24.32 ± 18.34 W m^{-2} (BOA SW), −16.03 ± 13.44 W m^{-2} (TOA SW), 5.51 ± 3.47 W m^{-2} (BOA LW), and 2.15 ± 1.31 W m^{-2} (TOA LW), while the mean radiative forcing values found without mineral dust before the lockdown are clearly lower: −11.04 ± 2.37 W m^{-2} (a decrease of about 54.60%), −3.73 ± 1.80 W m^{-2} (76.73%), 1.54 ± 0.79 W m^{-2} (72.05%), and 0.27 ± 0.27 W m^{-2} (87.44%) for the morning cases and −12.60 ± 6.91 W m^{-2} (48.19%), −4.92 ± 3.40 W m^{-2} (69.31%), 2.16 ± 1.23 W m^{-2} (60.80%), and 0.63 ± 0.42 W m^{-2} (70.69%) for the afternoon cases. The differences found between the dust cases and the afternoon cases are lower than the differences between the dust cases and the morning cases due to the activities that cause an increase of AOD during the day and the increase of the ST due to the solar radiation. During the lockdown, the mean radiative forcing values and their standard deviation are about −8.65 ± 0.77 W m^{-2}, −2.50 ± 0.87 W m^{-2}, 1.30 ± 1.18 W m^{-2}, 0.50 ± 0.43 W m^{-2} for the morning cases and −10.53 ± 3.12 W m^{-2}, −4.76 ± 2.18 W m^{-2}, 3.23 ± 2.04 W m^{-2} and 1.63 ± 0.92 W m^{-2} for the afternoon cases.

The mean AOD_{440} retrieved by the AERONET sun photometer before the lockdown are about 0.08 ± 0.04 and 0.10 ± 0.06 and during the lockdown 0.06 ± 0.01 and 0.08 ± 0.02 for the morning and afternoon cases respectively, which corresponds to a decrease between 20 and 25%. In turn, the mean SSA_{440} values are about 0.83 ± 0.06 and 0.89 ± 0.02 for the morning cases before and during lockdown, respectively, and 0.84 ± 0.08 and 0.91 ± 0.06 for the afternoon cases, indicating a decrease not only in the aerosol load but also in the more absorbing aerosol types. It is worth to note the behavior observed in the fine-mode-fraction, which in general is greater than the fine-mode-fraction of Table 3, since before the lockdown period the mean values are 0.76 ± 0.15 and 0.69 ± 0.14 for the morning and afternoon cases respectively while during the lockdown period those mean values are 0.66 ± 0.07 and 0.66 ± 0.11. There is a clear decrease in the morning cases caused by the decrease of the human activities, since anthropogenic aerosols AOD is dominated by fine aerosols [64], during the lockdown but in the afternoon cases the mean value is very similar, but still lower during the lockdown, because of the influence of case 12a that presents a very low fine-mode-fraction, possibly affected by the first Saharan dust event detected during the first days of lockdown.

Figure 5 shows the radiative forcing estimates in the SW spectral range at the BOA and at the TOA for the morning and afternoon cases before and during the lockdown. One can observe that the mean cooling effect during the lockdown is clearly lower, at the BOA, than before it, as much as for the morning cases as the afternoon cases (21.65% and 16.43%, respectively) because of the decrease in the AOD commented above and also observed in Figure 4. For the morning cases, at the TOA, the cooling effect is also lower during the lockdown (32.98%); however, for the afternoon cases, the mean cooling effect is just 3.25% lower. This result is related to the absorption and scattering, both the AOD_{440} and the SSA_{440} are greater in the afternoon than in the morning and therefore in the afternoon the scattering processes by the aerosol particles dominate with respect to the absorption ones causing an increase in the cooling effect [16].

Figure 6 shows the LW radiative forcing estimates at the BOA and at the TOA for the morning and afternoon cases before and during the lockdown in Spain. At the BOA, the radiative forcing estimates present, on average, a heating effect during the lockdown lower than before it for the morning cases, 15.52%. At the surface, the LW radiative forcing is strongly affected by the AOD, for instance, differences about 33% in the AOD can lead in some situations to a difference of about 4 W m^{-2} (see Figure 7a in [2]). Therefore, the observed difference in the morning cases in the present work can be explained by means of the sharp decrease (about 20%) in the AOD_{440} noticed above. At the TOA for the morning cases, the heating effect is now greater during the lockdown than before, about 45.45%, an opposite behavior than that at the surface because at the TOA the radiative forcing in the LW spectral range is mostly affected by the ST (see Figure 7a,f in [2]), where an increase of 11.58% can lead to an increase of about 5 W m^{-2}. In the present work, the average ST before the lockdown is

about 277.00 ± 3.88 K while during the lockdown the average ST is about 290.39 ± 6.34 K, showing an increase around 4.61%. For the afternoon cases, both at the BOA and at the TOA, the heating effect is on average greater during the lockdown than before (33.12% and 61.54% respectively). At the TOA this behavior again is attributable to the increase of the average ST from 286.46 ± 5.00 K to 301.53 ± 9.49 K as in the morning cases. However at the BOA, where the influence of the ST in the LW radiative forcing is much lower than at the TOA and variations in the AOD are directly related to variations in the radiative forcing [2], there is a decrease in the AOD_{440} around a 25% that cannot explain the increase of the heating effect. This increase in the heating effect is due to three cases—17a (18 May), 18a (19 May), and 19a (20 May)—that present LW radiative forcing values more than 2 times greater than the rest of the lockdown cases. That is because of their absorbing properties (SSA_{440} values of 0.90, 0.88 and 0.81) that cause an increase in the LW radiative forcing [2,14], while the aerosols present in the atmosphere during the previous days were less absorbing (SSA_{440} values around 0.96). As the AOD_{440} and asy_{440} present similar values in these three cases with respect to the rest of the lockdown cases, a more detailed research including aerosol typing and aging is needed in order to clarify what happened in the atmosphere during the third week of May.

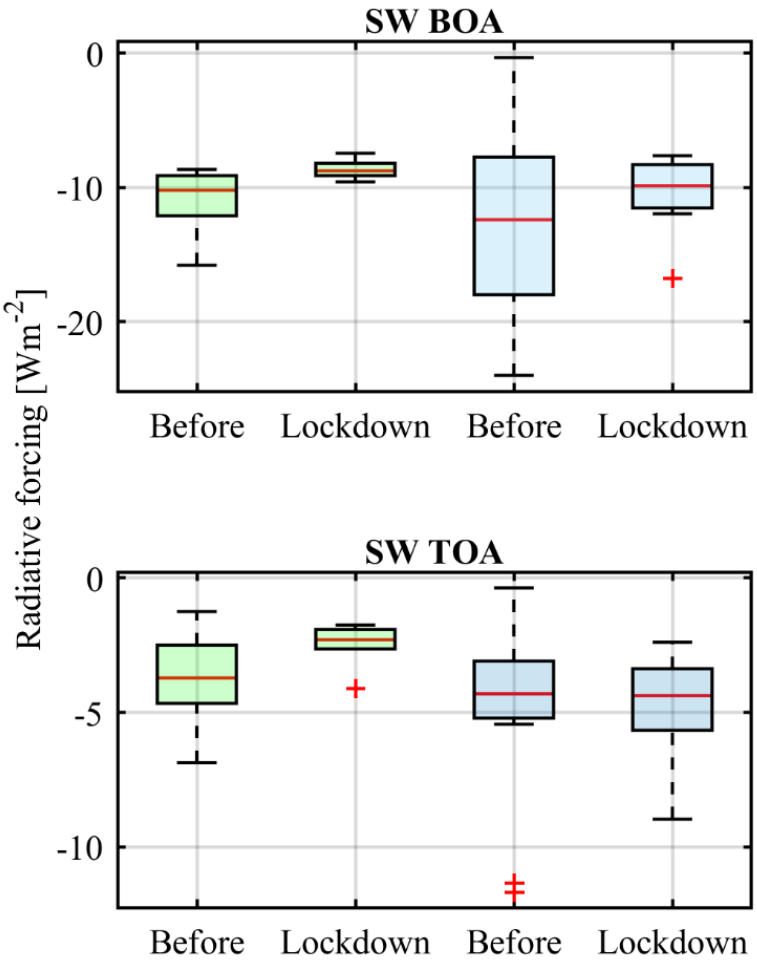

Figure 5. Boxplot of the aerosol radiative forcing in the SW spectral range estimated at the BOA (upper figure) and at the TOA (lower figure) for the morning (green boxes) and afternoon (blue boxes) before and during lockdown cases. Red lines inside the boxes stand for the median value in each scenario, the lower and upper limits of each box represent the 25th and 75th percentile respectively and black horizontal lines extend to the most extreme radiative forcing estimates not considered outliers. Red crosses represent the radiative forcing estimates considered as outliers.

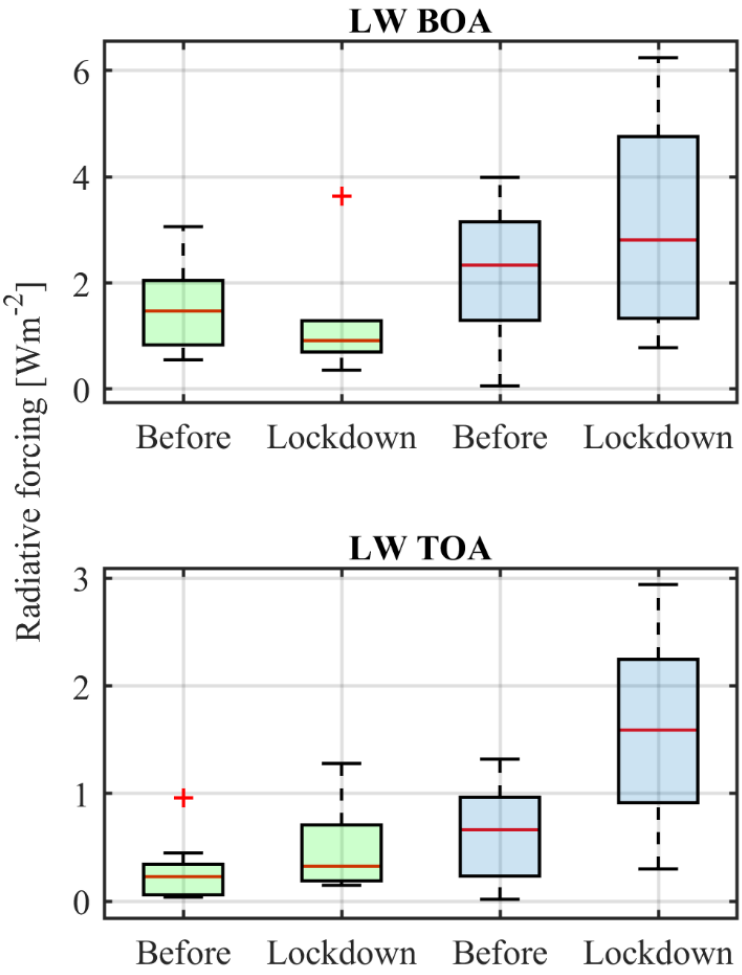

Figure 6. Boxplot of the aerosol radiative forcing in the LW spectral range estimated at the BOA (upper figure) and at the TOA (lower figure) for the morning (green boxes) and afternoon (blue boxes) before and during lockdown cases. Red lines inside the boxes stand for the median value in each scenario, the lower and upper limits of each box represent the 25th and 75th percentile respectively and black horizontal lines extend to the most extreme radiative forcing estimates not considered outliers. Red crosses represent the radiative forcing estimates considered as outliers.

In addition, the Mann–Whitney test has been applied to check the statistical significance of the observed differences between the medians of the radiative forcing values data sets before and during the lockdown. Thus, eight different tests named T1, T2, T3, T4, T5, T6, T7, and T8 have been performed. T1, T2, T3, and T4 are the tests made for the morning cases in the SW spectral range at the BOA (T1) and at the TOA (T2) and in the LW spectral range at the BOA (T3) and at the TOA (T4). T5, T6, T7, and T8 are the tests for the afternoon cases. Therefore, getting $p < 0.05$ from the Mann–Whitney test implies that the differences between the variables are significant at 95% confidence level. Table 6 sums up the p values for the eight cases.

Only in two tests (T1 and T8) the differences in the medians of the radiative forcing values before and during the lockdown can be considered statistically significant. In the case of the SW radiative forcing at the BOA estimated in the morning, there is a huge decrease in the cooling effect during the lockdown because of the decrease of AOD as has been aforementioned, causing a statistically significant difference between the radiative forcing values estimated before and during the lockdown (T1). T8 shows that the greater temperature found during the lockdown cases than before added to the presence of absorbing particles in the atmosphere lead to a statistically significant increase of the heating effect.

Table 6. Median, 25th, and 75th percentiles and p values from the Mann–Whitney analysis for the 8 comparisons. The superscripts in the p values stand for the test names.

	MorningCases [W m^{-2}]				AfternoonCases [W m^{-2}]			
	Median	**25th perc.**	**75th perc.**	p	**Median**	**25th perc.**	**75th perc.**	p
BOA SW before	−10.21	−12.11	−9.12	$^{T1}0.02$	−12.42	−18.01	−7.75	$^{T5}0.37$
BOA SW lockdown	−8.77	−9.12	−8.20		−9.89	−11.53	−8.30	
TOA SW before	−3.72	−4.66	−2.49	$^{T2}0.25$	−4.31	−5.21	−3.09	$^{T6}0.89$
TOA SW lockdown	−2.29	−2.64	−1.92		−4.38	−5.67	−3.38	
BOA LW before	1.47	0.83	2.05	$^{T3}0.39$	2.34	1.29	3.15	$^{T7}0.25$
BOA LW lockdown	0.92	0.70	1.29		2.81	1.34	4.76	
TOA LW before	0.23	0.06	0.35	$^{T4}0.23$	0.67	0.24	0.97	$^{T8}0.02$
TOA LW lockdown	0.33	0.19	0.71		1.59	0.92	2.25	

Tables 4 and 5 and Figures 5 and 6 show the presence of radiative forcing values considered as outliers by the box plots in some of the 16 scenarios. Concretely these six outliers, marked in bold in Tables 4 and 5 and red crosses in Figures 5 and 6, correspond to case 11m in the LW spectral range at the TOA (+0.96 W m^{-2}), case 14m in the SW at the TOA (−4.11 W m^{-2}), case 18m in the LW at the BOA (+3.64 W m^{-2}), case 3a in the SW at the TOA (−11.69 W m^{-2}), case 4a in the SW at the TOA (−11.36 W m^{-2}), and case 13a in the SW at the BOA (−16.80 W m^{-2}). The presence of these outliers causes an increase in the probability of getting a value greater than the value computed by the test and, hence, increasing p, for instance, the two statistically significant tests do not present outliers in Figures 5 and 6. By excluding the outliers from the five tests affected (T2, T3, T4, T5, and T6), the p values show a strong decrease from 0.25, 0.39, 0.23, 0.37 and 0.89 to 0.11, 0.11, 0.13, 0.24, and 0.41 for T2, T3, T4, T5, and T6 respectively. However, in spite of this behavior, the test Mann–Whitney is still showing that only T1 and T8 present statistically significant differences.

Furthermore, the radiative forcing depends in both spectral ranges, SW and LW, on the solar zenith angle and the AOD. The latter has been diminished because of the lockdown, however, the effect of the two Saharan dust intrusions detected during the lockdown period added to the light decrease in the AOD observed in Figure 4 and the small amount of data available due to the exceptional situation lead to statistically non-significant differences in the radiative forcing. In spite of the statistically non-significant differences, the results point out that the observed variations in the radiative forcing are directly related to the decrease of direct pollutant emissions and the consequent reduction of ambient aerosols in Madrid air basin.

5. Conclusions

This work has checked the feasibility of using ceilometer signals at 1064 nm to calculate radiative properties under different air pollution conditions in Madrid, Spain. In first place, the estimation of backscattering coefficient profiles from ceilometer signals by means of the Klett–Fernald inversion method was validated, thus five of the six selected cases fulfill the imposed criteria; just one case has shown a *NMB* value greater than the chosen threshold because of the presence of clouds at 2 km. Assuming that these result can lead to the estimation of reliable extinction coefficient profiles from ceilometer measurements, then, these profiles were estimated from selected measurements since January to May, and used in combination with AERONET and COPERNICUS data to feed the GAME radiative transfer model. First, African dust radiative forcing values were estimated in eight different cases, showing all the cases negative values at all levels in the SW spectral range (cooling effect of the aerosol) and positive values in the LW spectral range (heating effect) as in the literature. Besides, the range of the radiative forcing estimates was in agreement with the literature for similar values of AOD and SSA. The results also showed that, at one with previous works, high values of AOD imply high radiative effects as high values of θ_z imply a decrease in the cooling effect independently of the AOD. To the best of our knowledge, this is one of the first studies in which ceilometer measurements at 1064 nm can be successfully used for performing 1-D aerosol radiative forcing calculations, obtaining reliable results.

Then, after these reliable results the ceilometer signals at 1064 nm have been analyzed to quantify the radiative forcing before and during the lockdown caused by the COVID-19 sanitary crisis in Madrid.

Thus, considering that during the lockdown period, in comparison to the 6 previous years, a decrease in the AOD_{440} has been observed over the measurement site and that ceilometer signals can be used to retrieve consistent radiative forcing values, a total of 37 radiative forcing calculations (18 morning and 19 afternoon cases) were performed with no presence of mineral dust before and during the lockdown. The obtained cooling effect in the SW spectral range at all levels and the heating effect in the LW at the BOA for the morning cases were lower during the lockdown than before because of the observed decrease in the AOD_{440}. However, in the LW at the BOA, for the afternoon cases the heating effect during the lockdown increased because of the presence of absorbing particles ($SSA_{440} \leq 0.90$) in the atmosphere. According to the work in [14], those particles have their origin in smoke and pollution, therefore it can be assumed that in the afternoon cases the accumulated pollution from the considered essential activities and industries are increasing the computed heating effect. During the lockdown, the afternoon scenarios present higher AOD values than the morning scenarios, causing lower differences between before and during the lockdown in the afternoon than in the morning because of the considered essential activities and industries.

In the LW at the TOA, variations in the ST imply a greater effect in the radiative forcing calculations than variations in the AOD, thus the observed increment in the ST causes a greater heating effect during the lockdown for the morning and afternoon cases than before.

Finally, from the statistical analysis, only two of the eight analyzed scenarios shown statistically significant differences between the radiative forcing values estimated before and during the lockdown. The first scenario ($p = 0.02$) was at the BOA in the SW spectral range for the morning cases, which is strongly influenced by variations in the AOD. The second scenario ($p = 0.02$) was at the TOA in the LW spectral range for the afternoon cases, where variations of ST lead to strong variations in the radiative forcing estimates. The statistically meaningless differences observed in the other six scenarios can be explained because of the presence of absorbing particles and other atmospheric interactions that can affect the radiative forcing, for instance wet removal of atmospheric aerosols by falling precipitation. However, the observed variations in the radiative forcing estimates in the SW and LW spectral ranges at all levels before and during the lockdown are directly related with the decrease of emissions of aerosols from human activities. Therefore, the lockdown measures imposed due to the sanitary crisis lived in Spain have had an impact on the radiation budget. This information can be used for proposing action plans destined to reduce the impact of aerosols in radiative forcing in metropolitan areas with a high population density, such as Madrid, and consequently to improve the current knowledge of their influence on climate change.

Author Contributions: Conceptualization, R.B. and F.M.; methodology, R.B., F.M., M.J.G.-M., and P.S.; software, R.B. and M.J.G.-M.; validation, R.B.; formal analysis, R.B. and P.S.; investigation, R.B.; resources, R.B. and F.M.; data curation, R.B. and F.M.; writing—original draft preparation, R.B.; writing—review and editing, R.B., F.M., M.J.G.-M., P.S., M.P., and B.A.; project administration, B.A.; funding acquisition, M.P. and B.A. All authors have read and agreed to the published version of the manuscript.

Funding: This work was supported by H2020 programme from the European Union (grant 654109, ACTRIS-2 project and grant 871115, ACTRIS IMP project), the Spanish Ministry of Economy and Competitivity (CRISOL, CGL2017-85344-R) and Madrid Regional Government (TIGAS-CM, Y2018/EMT-5177). Maria J. Granados-Muñoz is funded by a Maria Sklodowska-Curie IF under grant agreement no. 796539.

Acknowledgments: The authors would like to acknowledge to ACTRIS-SPAIN (CGL2017-90884-REDIT), coordinated by Granada University, for providing quality-assured aerosol measurements and acknowledge to AERONET and COPERNICUS Global Land Services for sun-photometer and satellite quality-assured data processing and distribution. The authors also acknowledge to the Atmospheric Modelling & Weather Forecasting Group in the University of Athens, the Earth Science Dpt. from the Barcelona Supercomputing Centre and the Naval Research laboratory for the provision of SKIRON, DREAM/BSCDREAM8b and NAAPs aerosol maps, respectively. Philippe Dubuisson, the developer of the GAME code, is specially acknowledged. Furthermore, the developers of the HYSPLIT model are also acknowledged. The task of identifying African dust events and quantifying the dust contribution in the regions of the Spanish territory has been routinely carried out in the framework of projects funded by the Spanish ministry for the Ecological Transition (MITECO).

Conflicts of Interest: The authors declare no conflict of interest.

References

1. Barragan, R.; Sicard, M.; Totems, J.; Léon, J.F.; Dulac, F.; Mallet, M.; Pelon, J.; Alados-Arboledas, L.; Amodeo, A.; Augustin, P.; et al. Spatio-temporal monitoring by ground-based and air- and space-borne lidars of a moderate Saharan dust event affecting southern Europe in June 2013 in the framework of the ADRIMED/ChArMEx campaign. *Air Qual. Atmos. Heal.* **2017**, *10*, 261–285. [CrossRef]
2. Sicard, M.; Bertolín, S.; Mallet, M.; Dubuisson, P.; Comerón, A. Estimation of mineral dust long-wave radiative forcing: Sensitivity study to particle properties and application to real cases in the region of Barcelona. *Atmos. Chem. Phys.* **2004**, *14*, 9213–9231. [CrossRef]
3. Ricchiazzi, P.; Yang, S.; Gautier, C.; Sowle, D. SBDART: A research and teaching software tool for plane-parallel radiative transfer in the Earth's atmosphere. *Bull. Am. Meteorol. Soc.* **1998**, *79*, 2101–2114. [CrossRef]
4. Key, J.; Schweiger, A.J. Tools for atmospheric radiative transfer: Streamer and FluxNet. *Comp. Geosci.* **1998**, *24*, 443–451. [CrossRef]
5. Berk, A. MODTRAN5: 2006 update. In *Algorithms and Technologies for Multispectral, Hyperspectral and Ultraspectral Imagery XII*; International Society for Optics and Photonics: Orlando, FL, USA, 2006; Volume 6233, p. 62331F.
6. Mayer, B.; Kylling, A. Technical note: The libRadtran software package for radiative transfer calculations—Description and examples of use. *Atmos. Chem. Phys.* **2005**, *5*, 1855–1877. [CrossRef]
7. Dubuisson, P.; Dessailly, D.; Vesperini, M.; Frouin, R. Water vapor retrieval over ocean using near-infrared radiometry. *J. Geophys. Res.* **2004**, *109*, D19106. [CrossRef]
8. Dubuisson, P.; Roger, J.; Mallet, M.; Dubovik, O. A code to compute the direct solar radiative forcing: Application to anthropogenic aerosols during the Escompte Experiment. In Proceedings of the International Radiation Symposium (IRS 2004) on Current Problems in Atmospheric Radiation, Busan, Korea, 23–28 August 2004; pp. 127–130.
9. Granados-Muñoz, M.J.; Sicard, M.; Román, R.; Benavent-Oltra, J.A.; Barragán, R.; Brogniez, G.; Denjean, C.; Mallet, M.; Formenti, P.; Torres, B.; et al. Impact of mineral dust on shortwave and longwave radiation: Evaluation of different vertically resolved parameterizations in 1-D radiative transfer computations. *Atmos. Chem. Phys.* **2019**, *19*, 523–542. [CrossRef]
10. Granados-Muñoz, M.J.; Sicard, M.; Papagiannopoulos, N.; Barragan, R.; Bravo-Aranda, J.A.; Nicolae, D. Two-dimensional mineral dust radiative effect calculations from CALIPSO observations over Europe. *Atmos. Chem. Phys.* **2019**, *19*, 13157–13173. [CrossRef]
11. Mallet, M.; Pont, V.; Liousse, C.; Roger, J.C.; Dubuisson, P. Simulation of aerosol radiative properties with the ORISAM-RAD model during a pollution event (ESCOMPTE 2001). *Atmos. Environ.* **2006**, *40*, 7696–7705. [CrossRef]
12. Mallet, M.; Dulac, F.; Formenti, P.; Nabat, P.; Sciare, J.; Roberts, G.; Pelon, J.; Ancellet, G.; Tanré, D.; Parol, F.; et al. Overview of the chemistry-aerosol Mediterranean experiment/aerosol direct radiative forcing on the Mediterranean climate (ChArMEx/ADRIMED) summer 2013 campaign. *Atmos. Chem. Phys.* **2016**, *16*, 455–504. [CrossRef]
13. Perrone, M.R.; Tafuro, A.M.; Kinne, S. Dust layer effects on the atmospheric radiative budget and heating rate profiles. *Atmos. Environ.* **2012**, *59*, 344–354. [CrossRef]
14. Sicard, M.; Mallet, M.; García-Vizcaíno, D.; Comerón, A.; Rocadenbosch, F.; Dubuisson, P.; Muñoz-Porcar, C. Intense dust and extremely fresh biomass burning in Barcelona, Spain: Characterization of their optical properties and estimation of their radiative forcing. *Environ. Res. Lett.* **2012**, *7*, 034016. [CrossRef]
15. Romano, S.; Burlizzi, P.; Perrone, M.R. Experimental determination of short- and long-wave dust radiative effects in the central Mediterranean and comparison with model results. *Atmos. Res.* **2016**, *171*, 5–20. [CrossRef]
16. Barragan, R.; Romano, S.; Sicard, M.; Burlizzi, P.; Perrone, M.R.; Comeron, A. Estimation of mineral dust direct radiative forcing at the EARLINET site of Lecce, Italy, during the ChArMEx/ADRIMED summer 2013 campaign: Impact of radiative transfer model spectral resolutions. *J. Geophys. Res.* **2016**, 121. [CrossRef]

17. Meloni, D.; di Sarra, A.; Brogniez, G.; Denjean, C.; De Silvestri, L.; Di Iorio, T.; Formenti, P.; Gómez-Amo, J.L.; Gröbner, J.; Kouremeti, N.; et al. Determining the infrared radiative effects of Saharan dust: A radiative transfer modelling study based on vertically resolved measurements at Lampedusa. *Atmos. Chem. Phys.* **2018**, *18*, 4377–4401. [CrossRef]
18. Holben, B.N.; Eck, T.F.; Slutsker, I.; Tanré, D.; Buis, J.P.; Setzer, A.; Vermote, E.; Reagan, J.A.; Kaufman, Y.J.; Nakajima, T.; et al. AERONET—A federated instrument network and data archive for aerosol characterization. *Remote Sens. Environ.* **1998**, *66*, 1–16. [CrossRef]
19. Giles, D.M.; Sinyuk, A.; Sorokin, M.G.; Schafer, J.S.; Smirnov, A.; Slutsker, I.; Eck, T.F.; Holben, B.N.; Lewis, J.R.; Campbell, J.R.; et al. Advancements in the Aerosol Robotic Network (AERONET) Version 3 database—automated near-real-time quality control algorithm with improved cloud screening for Sun photometer aerosol optical depth (AOD) measurements. *Atmos. Meas. Tech.* **2019**, *12*, 169–209. [CrossRef]
20. Sinyuk, A.; Holben, B.N.; Eck, T.F.; Giles, D.M.; Slutsker, I.; Korkin, S.; Schafer, J.S.; Smirnov, A.; Sorokin, M.; Lyapustin, A. The AERONET Version 3 aerosol retrieval algorithm, associated uncertainties and comparisons to Version 2. *Atmos. Meas. Tech.* **2020**, *13*, 3375–3411. [CrossRef]
21. Pappalardo, G.; Amodeo, A.; Apituley, A.; Comeron, A.; Freudenthaler, V.; Linné, H.; Ansmann, A.; Bösenberg, J.; D'Amico, G.; Mattis, I.; et al. EARLINET: Towards an advanced sustainable European aerosol lidar network. *Atmos. Meas. Tech.* **2014**, *7*, 2389–2409. [CrossRef]
22. Winker, D.M.; Pelon, J.R.; McCormick, M.P. CALIPSO mission: Spaceborne lidar for observation of aerosols and clouds. In *Lidar Remote Sensing for Industry and Environment Monitoring III*; International Society for Optics and Photonics: San Diego, CA, USA, 2003; Volume 4893, pp. 1–11. [CrossRef]
23. Omar, A.; Liu, Z.; Vaughan, M.; Thornhill, K.; Kittaka, C.; Ismail, S.; Hu, Y.; Chen, G.; Powell, K.; Winker, D.; et al. Extinction-to-backscatter ratios of Saharan dust layers derived from in situ measurements and CALIPSO overflights during NAMMA. *J. Geophys. Res. Atmos.* **2010**, *115*, D24217. [CrossRef]
24. Remer, L.A.; Kaufman, Y.J.; Tanré, D.; Mattoo, S.; Chu, D.A.; Martins, J.V.; Li, R.-R.; Ichoku, C.; Levy, R.C.; Kleidman, R.G.; et al. The MODIS Aerosol Algorithm, Products, and Validation. *J. Atmos. Sci.* **2005**, *62*, 947–973. [CrossRef]
25. Huang, J.; Fu, Q.; Su, J.; Tang, Q.; Minnis, P.; Hu, Y.; Yi, Y.; Zhao, Q. Taklimakan dust aerosol radiative heating derived from CALIPSO observations using the Fu-Liou radiation model with CERES constraints. *Atmos. Chem. Phys.* **2009**, *9*, 4011–4021. [CrossRef]
26. Lemaître, C.; Flamant, C.; Cuesta, J.; Raut, J.-C.; Chazette, P.; Formenti, P.; Pelon, J. Radiative heating rates profiles associated with a springtime case of Bodélé and Sudan dust transport over West Africa. *Atmos. Chem. Phys.* **2010**, *10*, 8131–8150. [CrossRef]
27. Bhawar, R.L.; Lee, W.-S.; Rahul, P.R.C. Aerosol types and radiative forcing estimates over East Asia. *Atmos. Environ.* **2016**, *141*, 532–541. [CrossRef]
28. Oikawa, E.; Nakajima, T.; Inoue, T.; Winker, D. A study of the shortwave direct aerosol forcing using ESSP/CALIPSO observation and GCM simulation. *J. Geophys. Res. Atmos.* **2013**, *118*, 3687–3708. [CrossRef]
29. Oikawa, E.; Nakajima, T.; Winker, D. An evaluation of the shortwave direct aerosol radiative forcing using CALIOP and MODIS observations. *J. Geophys. Res. Atmos.* **2018**, *123*, 1211–1233. [CrossRef]
30. Welton, E.J.; Campbell, J.R.; Spinhirne, J.D.; Scott, V.S. Global monitoring of clouds and aerosols using a network of micro-pulse lidar systems. In *Lidar Remote Sensing for Industry and Environmental Monitoring*; Singh, U.N., Itabe, T., Sugimoto, N., Eds.; International Society for Optics and Photonics: San Diego, CA, USA, 2001; Volume 4153, pp. 151–158.
31. Heese, B.; Flentje, H.; Althausen, D.; Ansmann, A.; Frey, S. Ceilometer lidar comparison: Backscatter coefficient retrieval and signal-to-noise ratio determination. *Atmos. Meas. Tech.* **2010**, *3*, 1763–1770. [CrossRef]
32. IQAir. *COVID-19 Air Quality Report*; IQAir: Goldach, Switzerland, 2020; p. 15. Available online: https://www.iqair.com/blog/air-quality/report-impact-of-covid-19-on-global-air-quality-earth-day (accessed on 16 September 2020).
33. Ministerio de la Presidencia, Relaciones con las Cortes y Memoria Democrática. Real Decreto 463/2020 de 14 de Marzo, por El que se Declara el Estado de Alarma para la Gestión de la Situación de Crisis Sanitaria Ocasionada por el COVID-19. 2020. Available online: https://www.boe.es/buscar/doc.php?id=BOE-A-2020-3692 (accessed on 17 September 2020).

34. Ministerio de la Presidencia, Relaciones con las Cortes y Memoria Democrática. Real Decreto-ley 10/2020, de 29 de Marzo, por El que se Regula un Permiso Retribuido Recuperable para las Personas Trabajadoras por Cuenta Ajena que no Presten Servicios Esenciales, con el Fin de Reducir la Movilidad de la Población en el Contexto de la Lucha Contra el COVID-19. 2020. Available online: https://www.boe.es/buscar/doc.php?id=BOE-A-2020-4166 (accessed on 17 September 2020).
35. Baldasano, J.M. COVID-19 lockdown effects on air quality by NO2in the cities of Barcelona and Madrid. *Sci. Total Environ.* **2020**, *741*. [CrossRef]
36. Tobias, A.; Carnerero, C.; Reche, C.; Massagué, J.; Viana, M.; Minguillón, M.C.; Alastuey, A.; Querol, X. Changes in air quality during the lockdown in Barcelona (Spain) one month into the SARS-CoV-2 epidemic. *Sci. Total Environ.* **2020**, 726. [CrossRef]
37. IPCC: Climate Change. *The Physical Science Basis, Contribution of Working Group I to the UN IPCC's Fifth Assessment Report*; Cambridge University Press: New York, NY, USA, 2013.
38. Fernandez, A.J.; Sicard, M.; Costa, M.J.; Guerrero-Rascado, J.L.; Gómez-Amo, J.L.; Molero, F.; Barragan, R.; Basart, S.; Bortoli, D.; Bedoya-Velásquez, A.E.; et al. Extreme, wintertime Saharan dust intrusion in the Iberian Peninsula: Lidar monitoring and evaluation of dust forecast models during the February 2017 event. *Atmos. Res.* **2018**, *228*, 223–241. [CrossRef]
39. Cazorla, A.; Casquero-Vera, J.A.; Román, R.; Guerrero-Rascado, J.L.; Toledano, C.; Cachorro, V.E.; Orza, J.A.; Cancillo, M.L.; Serrano, A.; Titos, G.; et al. Near-real-time processing of a ceilometer network assisted with sun-photometer data: Monitoring a dust outbreak over the Iberian Peninsula. *Atmos. Chem. Phys.* **2017**, *17*, 11861–11876. [CrossRef]
40. Klett, J.D. Stable analytic inversion solution for processing lidar returns. *Appl. Opt.* **1981**, *20*, 211–220. [CrossRef] [PubMed]
41. Klett, J.D. Lidar inversion with variable backscatter/extinction ratios. *Appl. Opt.* **1985**, *24*, 1638–1643. [CrossRef] [PubMed]
42. Fernald, F.G.; Herman, B.M.; Reagan, J.A. Determination of aerosol height distributions by lidar. *J. Appl. Meteorol.* **1972**, *11*, 482–489. [CrossRef]
43. Fernald, F.G. Analysis of atmospheric lidar observations: Some comments. *Appl. Opt.* **1984**, *23*, 652–653. [CrossRef] [PubMed]
44. Schmid, B.; Michalsky, J.; Halthore, R.; Beauharnois, M.; Harrison, L.; Livingston, J.; Russell, P.; Holben, B.; Eck, T.; Smirnov, A. Comparison of aerosol optical depth from four solar radiometers during the fall 1997 ARM intensive observation period. *Geophys. Res. Lett.* **1999**, *26*, 2725–2728. [CrossRef]
45. Dubovik, O.; King, M.D. A flexible inversion algorithm for retrieval of aerosol optical properties from Sun and sky radiance measurements. *J. Geophys. Res. Atmos.* **2000**, *105*, 20673–20696. [CrossRef]
46. Molero, F.; Jaque, F. The laser as a tool in environmental problems. *Opt. Mater.* **1999**, *13*, 167–173. [CrossRef]
47. Bodhaine, B.A.; Wood, N.B.; Dutton, E.G.; Slusser, J.R. On Rayleigh optical depth calculations. *J. Atmos. Ocean Tech.* **1999**, *16*, 1854–1861. [CrossRef]
48. Stamnes, K.; Tsay, S.C.; Wiscombe, W.; Jayaweera, K. Numerically stable algorithm for discrete-ordinate-method radiative transfer in multiple scattering and emitting layered media. *Appl. Opt.* **1988**, *27*, 2502–2509. [CrossRef]
49. Sicard, M.; Bertolín, S.; Muñoz-Porcar, C.; Rodríguez, A.; Rocadenbosch, F.; Comerón, A. Separation of aerosol fine- and coarse-mode radiative properties: Effect on the mineral dust longwave, direct radiative forcing. *Geophys. Res. Lett.* **2014**, *41*, 6978–6985. [CrossRef]
50. Krekov, G.M. Models of atmospheric aerosols. In *Aerosol Effects on Climate*; Jennings, S.G., Ed.; University of Arizona Press: Tucson, AZ, USA, 1993; pp. 9–72.
51. Roger, J.C.; Mallet, M.; Dubuisson, P.; Cachier, H.; Vermote, E.; Dubovik, O.; Despiau, S. A synergetic approach for estimating the local direct aerosol forcing: Application to an urban zone during the Experience sur Site pour Contraindre les Modèles de Pollution et de Transport d'Emission (ESCOMPTE) experiment. *J. Geophys. Res.* **2006**, *111*, D13208. [CrossRef]
52. Escudero, M.; Castillo, S.; Querol, X.; Avila, A.; Alarcón, M.; Viana, M.M.; Alastuey, A.; Cuevas, E.; Rodríguez, S. Wet and dry African dust episodes over eastern Spain. *J. Geophys. Res.* **2005**, *110*, D18S08. [CrossRef]

53. Salvador, P.; Artíñano, B.; Molero, F.; Viana, M.; Pey, J.; Alastuey, A.; Querol, X. African dust contribution to ambient aerosol levels across Central Spain: Characterization of long-range transport episodes of desert dust. *Atmos. Res.* **2013**, *127*, 117–129. [CrossRef]
54. Commission Staff Working Paper, Establishing Guidelines for Demonstration and Subtraction of Exceedances Attributable to Natural Sources Under the Directive 2008/50/EC on Ambient Air Quality and Cleaner Air for Europe, Brussels. 2011. Available online: http://ec.europa.eu/environment/air/quality/ (accessed on 7 September 2020).
55. Escudero, M.; Querol, X.; Pey, J.; Alastuey, A.; Pérez, N.; Ferreira, F.; Alonso, S.; Rodríguez, S.; Cuevas, E. A methodology for the quantification of the net African dust load in air quality monitoring networks. *Atmos. Environ.* **2007**, *41*, 5516–5524. [CrossRef]
56. Querol, X.; Pey, J.; Pandolfi, M.; Alastuey, A.; Cusack, M.; Pérez, N.; Moreno, N.; Viana, M.; Mihalopoulos, N.; Kallos, G.; et al. African dust contributions to mean ambient PM10 mass-levels across the Mediterranean basin. *Atmos. Environ.* **2009**, *43*, 4266–4277. [CrossRef]
57. Viana, M.; Salvador, P.; Artíñano, B.; Querol, X.; Alastuey, A.; Pey, J.; Latz, A.J.; Cabañas, M.; Moreno, T.; García, S.; et al. Assessing the performance of methods to detect and quantify African dust in airborne particulates. *Environ. Sci. Technol.* **2010**, *44*, 8814–8820. [CrossRef]
58. Fernandez, A.J.; Molero, F.; Salvador, P.; Revuelta, A.; Becerril-Valle, M.; Gómez-Moreno, F.J.; Artíñano, B.; Pujadas, M. Aerosol optical, microphysical and radiative forcing properties during variable intensity African dust events in the Iberian Peninsula. *Atmos. Res.* **2017**, *196*, 129–141. [CrossRef]
59. Draxler, R.R.; Hess, G.D. An Overview of the HYSPLIT_4 Modelling System for Trajectories, Dispersion, and Deposition. 1998. Available online: http://citeseerx.ist.psu.edu/viewdoc/download?doi=10.1.1.453.8780&rep=rep1&type=pdf (accessed on 31 August 2020).
60. Seinfeld, J.H.; Pandis, S.N. *Atmospheric Chemistry and Physics: From Air Pollution to Climate Change*; Wiley & Sons Publisher: Hoboken, NJ, USA, 1998.
61. Cachorro, V.E.; Toledano, C.; Prats, N.; Sorribas, M.; Mogo, S.; Berjón, A.; Torres, B.; Rodrigo, R.; de la Rosa, J.; De Frutos, A.M. The strongest desert dust intrusion mixed with smoke over the Iberian Peninsula registered with Sun photometry. *J. Geophys. Res.* **2008**, *113*, D14S04. [CrossRef]
62. Liao, H.; Seinfeld, J. Radiative Forcing by mineral dust aerosols: Sensitivity to key variables. *J. Geophys. Res.* **1998**, *103*, 31637–31645. [CrossRef]
63. Highwood, E.; Haywood, J.; Silverstone, M.; Newman, S.M.; Taylor, J. Radiative properties and direct effect of Saharan dust measured by the C-130 aircraft during Saharan Dust Experiment (SHADE): 2. Terrestrial spectrum. *J. Geophys. Res.* **2003**, *108*, D188578. [CrossRef]
64. Kleidman, R.G.; O'Neill, N.T.; Remer, L.A.; Kaufman, Y.J.; Eck, T.F.; Tanre, D.; Dubovik, O.; Holben, B.N. Comparison of Moderate Resolution Imaging Spectroradiometer (MODIS) and Aerosol Robotic Network (AERONET) remote-sensingretrievals of aerosol fine mode fraction over ocean. *J. Geophys. Res.* **2005**, *110*, D22205. [CrossRef]